Journal of Materials Chemistry A

ROYAL SOCIETY OF CHEMISTRY

PAPER

View Article Online
View Journal | View Issue

Cite this: *J. Mater. Chem. A*, 2020, **8**, 2453

Achieving electronic structure reconfiguration in metallic carbides for robust electrochemical water splitting†

Lulu Qiao,‡[a] Anquan Zhu,‡[a] Weixuan Zeng,[a] Rui Dong,[a] Pengfei Tan,[a] Zhengping Ding,[cd] Peng Gao,[cde] Shuangyin Wang *[b] and Jun Pan *[a]

Developing transition metal carbides (TMCs) as multifunctional electrocatalysts to catalyze the oxygen evolution reaction (OER) and hydrogen evolution reaction (HER) has been attracting increasing attention. Unlike traditional single-source modification, a novel nitrogen-doped carbon-hosted TMC catalyst with dual transition metals to modulate the electronic structures of tungsten carbide is reported here. It enables implementation by introducing copper from a prefabricated core–shell $CuWO_4$@ZIF-67 precursor and subsequently with an annealing treatment, which not only maximize the active Co and W sites, but also enable the construction of a good interconnected conductive network. Consequently, the optimized nitrogen-doped carbon-supported polymetallic carbide catalyst synthesized at 700 °C (denoted as S-2) with a suitable structure and composition configuration exhibits decent activities with ultralow overpotentials (η) of 238 mV and 98 mV at 10 mA cm^{-2} for OER and HER, respectively, along with good overall water splitting performances, surpassing that of majority of TMCs. This work paves viable ways for the rational design and regulation of the local electron structures of metallic carbides by introducing appropriate transition metals.

Received 27th September 2019
Accepted 26th December 2019

DOI: 10.1039/c9ta10682k

rsc.li/materials-a

1. Introduction

By extensively implanting sustainable concepts into general concerns, the massive production of clean, high-energy and renewable molecular hydrogen (H_2) to replace traditional fossil energy through the electrocatalytic water splitting technology has been gradually earning widespread attention among public, especially in the fields of scientific research and industrialization. However, the problem is the practical implementation of this technology that severely depends on the two half-cell reactions involved, *viz.*, the hydrogen evolution reaction (HER) at the cathode and the oxygen evolution reaction (OER) at the anode.[1,2] Unfortunately, both these reactions are achieved under the conditions of an additionally high overpotential (η) and they are always limited by their sluggish dynamic mechanisms.[3–5] Herein, the required task for researchers is to develop appropriate nanostructures as catalyst electrodes to overcome these limitations and simultaneously contribute to favorable activity and durability. Currently, because of their prohibitive cost and low earth abundance, noble-metal Pt-based and Ru/Ir-based materials still cannot qualify as optimal catalysts for HER and OER for commercial and large-scale applications even though they generally exhibit superior catalytic activities for HER and OER than others.[6–8] Thus, the development of highly efficient and cost-effective alternative catalysts is eagerly desired.

Recently, a series of earth-abundant transition metal carbides (TMCs) have been investigated by devising new nanostructures and tailoring their electronic properties for HER and OER.[3,9–11] Some previous meaningful studies related to tungsten/molybdenum carbide-based catalysts indicate that these catalysts seem to be only active in HER because of their similar d-band electronic structure configuration to that of Pt species, but they generally have an inferior behavior when used as OER catalyst electrodes.[10,12–15] Meanwhile, the features including good thermal/chemical stability and low cost equip these catalysts with long-term operation durability in commercial practices.[16] However, the improvement in the HER activity for such catalysts is still restricted due to their strong surface hydrogen adsorption capacity.[17] Worse, the surface of tungsten/molybdenum carbide catalysts is prone to the irreversible

[a]State Key Laboratory for Powder Metallurgy, Central South University, Changsha, 410083, People's Republic of China. E-mail: jun.pan@csu.edu.cn

[b]State Key Laboratory of Chem/Bio-Sensing and Chemometrics, College of Chemistry and Chemical Engineering, Hunan University, Changsha, Hunan, 410082, P. R. China. E-mail: shuangyinwang@hnu.edu.cn

[c]International Center for Quantum Materials, School of Physics, Peking University, Beijing 100871, China

[d]Electron Microscopy Laboratory, School of Physics, Peking University, Beijing 100871, China

[e]Collaborative Innovation Center of Quantum Matter, Beijing 100871, China

† Electronic supplementary information (ESI) available. See DOI: 10.1039/c9ta10682k

‡ These authors contributed to this work equally.

adsorption of the OH* and O* intermediates in the water splitting process, leading to the blockage of active sites.[18] To deal with these problems, some optimized structures based on tungsten/molybdenum carbides have been synthesized and investigated. For example, strongly and externally coupled molybdenum/tungsten carbide phases with transition metals Ni and Co simultaneously integrated on carbon matrices have been developed as high-performance water splitting catalysts.[19–22] The authors attribute such high catalytic activity to a higher Ni/Co valence state and a lower Mo/W valence state, which are a result of the interface electron transfer from metallic Ni/Co to tungsten/molybdenum carbides. The adsorption/desorption energy of the reactant, intermediate, and product at the W/Mo and Ni/Co sites can be regulated to a moderate level, subsequently facilitating the water splitting processes. On the other hand, various kinds of polymetallic carbides (M_xN_xC, M = Co/Ni/Fe, N = Mo/W) have been demonstrated to be highly active and stable towards water splitting.[23–27] In our opinion, these M_xN_xC phases, also known as interstitial compounds, are actually a solid solution in which the solute metallic Co/Ni/Fe can be incorporated into the lattice spacing of tungsten/molybdenum carbides.[17] In this regard, efficient atomic contact can give rise to strong electronic interactions among different metallic atoms. Therefore, the electronic states of metallic elements can be rearranged. Still, the trouble is that even with the availability of highly active Co species, they are fairly not enough if metallic Co nanoparticles are inevitably reduced and randomly encompassed into carbon matrices instead of adjacent to tungsten/molybdenum carbides at a high reaction temperature.[21] Enlightened by the above-mentioned discussion, we considered the design and synthesis of a unique tungsten carbide-based nanostructure, simultaneously achieving more efficient electron transfer and promoting the utilization rate of active Co species as much as possible. We believe, if so, the electrocatalytic activity will be further boosted.

Generally speaking, the synthetic requirement of pure tungsten carbide is quite strict, with extremely elevated temperature conditions (above 1000 °C) and specific reductive atmospheres.[14,28] Spontaneously, the as-obtained tungsten carbides tend to congregate into bulky and agglomerated particles,[29] resulting in their dissatisfactory catalytic activity. Extensive research has validated the superiorities of using metal–organic framework (MOF) relatives as precursors to manufacture tungsten/molybdenum carbide-based nanostructures, including the decreased formation temperature of carbides and self-generated reductive amorphous carbon as well as its benign hosted and confined effect on inorganic nanoparticles.[30–33] More recently, Honggang Fu *et al.*[24] employed ZIF-67-trapped $[PMo_{12}O_{40}]^{3-}$ (PMo_{12}) clusters as the source material to successfully prepare small-sized Co_xMo_xC well-confined by the carbon host. They highlighted the above-mentioned advantages of carbides derived from MOF precursors.

Inspired by the aforementioned statements, the transition metal Cu with slightly higher electronegativity than metallic Co was selected and introduced from prefabricated core–shell $CuWO_4$@ZIF-67 precursors to develop multi-metal-modified tungsten carbide-based catalysts. This method aimed at realizing the maximum utilization of active Co sites, providing good conductors for electron transfer and regulating the electronic structures of tungsten carbide crystals. Based on the structural and compositional characterization results, the detailed transformation route corresponding to the W species is proposed. None of the metallic phase Co could be detected in the as-prepared samples. As expected, the nitrogen-doped carbon-supported polymetallic carbide catalyst synthesized at 700 °C (denoted as S-2) comprised metallic Cu, WC, Cu-doped Co_3W_3C, and nitrogen-doped carbon. Herein, the introduction of copper not only prevents cobalt from being randomly reduced to metallic Co nanoparticles in carbon matrices, but also helps achieve the partial replacement of the Co sites in Co_3W_3C. The S-2 catalyst as a multifunctional catalyst shows satisfactory electrochemical water splitting performances, with low overpotentials of 238 mV (at $j = 10$ mA cm^{-2}, j_{10}) for OER and 98 mV (j_{10}) for HER, which are even better than those of the commercial RuO_2 catalyst and comparable to those of the Pt/C catalyst in 1 M KOH solutions. Compared to other carbide catalysts, it still exhibits state-of-the-art performances (Tables S5, S7, and S8, ESI†). The active sites towards water splitting are also evaluated by the corresponding turnover frequency (TOF) calculations. Our work suggests that tailoring/modulating the electronic structure among various components is a promising way to devise high-activity carbide-based electrocatalysts for water splitting and other energy applications.

2. Experimental

2.1. Preparation of $CuWO_4$ nanoparticles

Typically, $CuWO_4$ nanoparticles were prepared through a two-step route, namely, the hydrothermal reaction followed by an annealing treatment. Above all, 4.11 g copper nitrate trihydrate ($Cu(NO_3)_2 \cdot 3H_2O$) was dissolved in 25 mL deionized water (named solution A) and then, 1 mL ammonium hydroxide ($NH_3 \cdot H_2O$) was added into solution A. Similarly, 5.345 g sodium tungstate dihydrate ($Na_2WO_4 \cdot 2H_2O$) was dispersed in 25 mL deionized water to form a homogeneous solution B. Then, solution B was added dropwise to solution A with electromagnetic agitation at room temperature. Subsequently, the pH value of the mixture was adjusted to 5.2 by the gradual addition of dilute nitric acid (HNO_3). After stirring for another 2 h, the blue suspension was transferred into 100 mL Teflon-lined stainless autoclave and kept at 180 °C for 20 h to obtain a green product. After facile centrifugation, washing, and drying procedures, the $CuWO_4 \cdot 2H_2O$ sample could be obtained. Finally, the as-prepared $CuWO_4 \cdot 2H_2O$ was calcinated at 500 °C at a heating rate of 5 °C min^{-1} and maintained for 2 h. Then, the $CuWO_4$ sample could be fabricated by centrifugation, washing, and drying at 60 °C for 15 h.

2.2. Preparation of core–shell $CuWO_4$@ZIF-67 and ZIF-67

Core–shell structural $CuWO_4$@ZIF-67 was used as the precursor to synthesize nitrogen-doped carbon-hosted polymetallic

carbide catalysts (S-1, S-2, and S-3). In a typical synthetic route of the $CuWO_4$@ZIF-67 core–shell structure, 40 mg $CuWO_4$ sample and 0.65 g 2-methylimidazole (2-MIM) were mixed in 40 mL methanol solution under ultrasonic treatment for 30 min (denoted as dispersed solution C). Solution D was prepared by dispersing 0.45 g cobalt chloride hexahydrate ($CoCl_2 \cdot 6H_2O$) into 10 mL methanol. Then, solution D was added dropwise into dispersed solution C at the rate of 500 μL min^{-1} *via* a peristaltic pump. After stirring and reacting for 20 h, the purple products were collected by centrifugation and washing with ethanol three times and eventually drying in a vacuum oven at 60 °C for 20 h. Similarly, ZIF-67 was prepared in the same way without the addition of the $CuWO_4$ sample.

2.3. Synthesis of nitrogen-doped carbon-hosted polymetallic carbide (NC@Cu-Co-W-C) catalysts

Taking equal amounts of the as-obtained $CuWO_4$@ZIF-67 precursor and putting it into a tube furnace with continuous argon flow, the temperature inside the tube was increased to 600, 700, and 800 °C at a heating rate of 5 °C min^{-1}, respectively, subsequently keeping the reaction temperature constant for 2 h. After cooling down to room temperature naturally, the as-obtained catalysts at 600, 700, and 800 °C were labeled as S-1, S-2, and S-3, respectively. For comparison, pure $CuWO_4$ and ZIF-67 were also treated under the same conditions as that for S-2 and named as S-4 and S-5.

3. Results and discussion

3.1. Structure and composition characterizations

As depicted in Fig. 1, the typical synthetic route of nitrogen-doped carbon-supported polymetallic carbide catalysts (NC@Cu-Co-W-C) can be divided into three parts. First of all, triclinic $CuWO_4$ nanoparticles with an average particle size of 97.5 nm (Fig. S3a, ESI†) were prepared by a two-step method consisting of the hydrothermal reaction and heat treatment. After this, a dispersed solution mixed with the $CuWO_4$ nanoparticles (NPs) and the organic ligand 2-methylimidazole (2-MIM) was subjected to ultrasonic treatment. This guaranteed the uniform distribution of $CuWO_4$ NPs along with the successful coordination between $CuWO_4$ NPs and 2-MIM. Once the metallic cobalt source was added to the above-mentioned dispersed solution, Co^{2+} ions could combine with 2-MIM that was already linked with $CuWO_4$ NPs, in turn forming ZIF-67 crystal layers tightly outside $CuWO_4$ NPs, *i.e.*, core–shell structures were developed. This is clearly demonstrated in Fig. S1 and S2 (ESI†). Compared with the XRD pattern of $CuWO_4$ NPs, several extra peaks in the XRD pattern of $CuWO_4$@ZIF-67 are assigned to ZIF-67. The morphology of the $CuWO_4$@ZIF-67 precursor can be observed in Fig. S2 (ESI†), which presents an obvious $CuWO_4$ NP core@ZIF-67 shell structure. Combined with the XRD result, we could reasonably determine the successful preparation of the core–shell $CuWO_4$@ZIF-67 precursor. In order to regulate the composition and structure of the final products, the $CuWO_4$@ZIF-67 precursor needs to undergo a thermal annealing process with a set of reaction temperatures. After being immersed in an argon atmosphere, the outer ZIF-67 and inner $CuWO_4$ NPs collectively experienced a series of complicated reactions at elevated temperatures, resulting in the development of several corresponding samples with diverse structures and compositions. Note that it is really a tough task to figure out the specific reaction and transformation processes related to the C, N, Co, W, and Cu elements. Alternatively, we can conclude a convincing reactive route based on the following structural and compositional characterizations. As we know, if the values of r_C/r_M (r_C is the atomic radius of a carbon atom and r_M represents the atomic radius of a metallic atom, including Co, W, and Cu) are more than 0.59, it tends to result in the formation of special interstitial compounds, such as Co_3W_3C and Co_6W_6C,[17,34] where Co atoms are actually incorporated into the lattice spacing of the WC phase. In consideration of the similar atomic radii of the transition metal Cu and Co atoms, it is highly possible to realize the substitution of Co atoms by Cu atoms in the reaction processes, thus getting the Cu-doped Co_xW_xC phases, which can supply numerous active sites for catalytic reactions and regulate the electron transfer direction. Located in an environment with abundant carbonaceous matrices, a core–shell Cu-doped Co_xW_xC/carbon layer structure is prone to forming during the reaction. These as-developed carbon shells not only prevent polymetallic carbide from agglomeration to larger particles, but also ensure satisfactory durability and good electrical conductivity throughout the electrochemical reactions.

To better understand the evolution of the component phases during the reaction processes at high temperatures, pure $CuWO_4$ NPs and ZIF-67 were also treated under the same preparation conditions as that for the S-2 sample. As displayed in Fig. S4 (ESI†), all the peaks in the XRD pattern of the S-4 sample match well with the PDF card (JCPDS 70-1732) of the triclinic $CuWO_4$ phase without any impurity peak, showing improved crystallinity. Clearly, the three peaks at around 44.2°, 51.5°, and 75.8° in the XRD pattern of the S-5 sample are assigned to the (111), (200), and (220) planes of cubic metallic Co (JCPDS 15-0806),[3] respectively. An extra broad peak at 26° is attributed to the (002) plane of graphitic carbon.[3] These facts indicate that the S-5 sample mainly comprises cubic Co and graphitic carbon. When taking the $CuWO_4$@ZIF-67 precursors as the reactants, the reactive processes would be relatively complicated. One interesting thing we find is that there are only peaks involved with cubic metallic Cu instead of cubic metallic Co detected in the whole XRD patterns of the S-1, S-2, and S-3

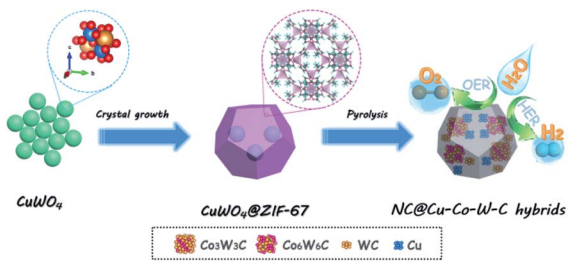

Fig. 1 Synthetic illustration of the NC@Cu-Co-W-C catalysts.

samples. This is caused by the more powerful metallicity of metallic Co compared to that of metallic Cu. When the reaction temperature is controlled at 600 °C, it is determined from the XRD curves (Fig. 2) that the primary phases of S-1 are monoclinic WO_2 (JCPDS 71-0614) and cubic metallic Cu (JCPDS 04-0836).[35] As the reaction temperature increases to 700 °C, monoclinic WO_2 is converted to hexagonal WC (JCPDS 73-0471)[36] and cubic Co_3W_3C (JCPDS 27-1125).[37] As pointed by Honggang Fu *et al.*,[24] the synthetic temperature of tungsten-based carbides is closely connected to the category of the carbon source and the contacting ways between the carbon source and the metal ions. Benefitting from the intact and delicate core–shell structure of the $CuWO_4$@ZIF-67 precursor, cubic Co_3W_3C can be formed at this low reaction temperature of 700 °C. For the S-2 sample, the three strong peaks that emerge at 31.5°, 35.6°, and 48.3° are associated with the (001), (100), and (101) planes of hexagonal WC, respectively.[36] In fact, the measured strongest peak position of cubic Co_3W_3C (that is the (511) plane) is 42.5° (Fig. S5a, ESI†), which is slightly positively shifted to a larger degree than that of the PDF standard (42.4°). This situation happens with other measured peaks of Co_3W_3C as well, suggesting the replacement of Co atoms in cubic Co_3W_3C with Cu atoms.[38] On the continual elevation of the reaction temperature to 800 °C, it is ascertained from the XRD pattern (S-3 sample) that hexagonal WC and cubic metallic Cu still exist. However, all the peaks related to cubic Co_3W_3C disappear; instead, there are new peaks corresponding to cubic Co_6W_6C (JCPDS 22-0597),[34] implying the phase transformation of the interstitial compounds from Co_3W_3C to Co_6W_6C induced by the increased reaction temperature. Analogous to Co_3W_3C, the recorded peak positions also shift slightly to larger degrees (Fig. S5b, ESI†). Given the more powerful metallicity of metallic Co than that of metallic Cu and based on the above-mentioned analysis, the possible reaction and conversion route can be proposed and summarized below (in view of the real reaction conditions, there might be little O_2 left in the tube):

$$600\ ^\circ\mathrm{C}:\ \mathrm{ZIF\text{-}67} + O_2 \rightarrow C + H_2O + CO_2 \quad (1)$$

$$CuWO_4 + C \rightarrow Cu + WO_3 + CO_2 \quad (2)$$

$$C + WO_3 \rightarrow WO_2 + CO_2 \quad (3)$$

$$700\ ^\circ\mathrm{C}:\ C + WO_2 \rightarrow W + CO_2 \quad (4)$$

$$C + W \rightarrow WC \quad (5)$$

$$WC + Co^{2+} + Cu^{2+} \rightarrow \text{Cu-doped } Co_3W_3C \quad (6)$$

$$800\ ^\circ\mathrm{C}:\ \text{Cu-doped } Co_3W_3C \rightarrow \text{Cu-doped } Co_6W_6C \quad (7)$$

XPS was conducted to probe into the surface chemical structures of the NC@Cu-Co-W-C catalysts. The survey spectra in Fig. 3a demonstrate the existence of C, N, Co, Cu, and W in all the as-synthesized samples. Further observations about specific chemical and electronic structures were made by high-resolution XPS spectra. For the C 1s HRXPS spectrum (Fig. 3b), the three peaks located at 284.8, 286.1, and 288.5 eV are assigned to the C–C/C=C, C–N/C–O, and O=C–O species, respectively,[10] implying the doping of nitrogen into the carbon skeletons. In addition to this, a special peak (283.1 eV) for both the S-2 and S-3 samples is detected, which corresponds to the C–W bonding structure, thus supporting the presence of the WC and Co_xW_xC compounds.[10,28] The successful N-doping into carbon can be confirmed by Fig. 3c, showing two dividing peaks at 398.7 eV (pyridinic N) and 400.8 eV (graphitic N). It was confirmed that the metallic valence states of the catalysts are closely related to their catalytic properties. Hence, we investigated the electronic structures of the Co, Cu, and W elements. In Fig. 3d, the peak position of Co $2p_{3/2}$ is made up of Co^{3+}, Co^{2+}, and Sat. (satellite peak), which indicates the fact that these oxidized Co species are associated with the interactions in the Cu-doped Co_xW_xC lattice.[3,24] It was found that the binding energy of Co^{3+} for the S-2 and S-3 samples increased to 781.0 eV from 780.7 eV of the S-1 sample; meanwhile, the $R(Co^{3+}/Co^{2+})$ value of S-2 was 1.96, and it was similar to that of S-3 (2.04) but much higher than that of S-1 (1.33). All these facts help conclude that the S-2 sample possesses more Co^{3+}, which is beneficial for water dissociation.[22] As for the Cu $2p_{3/2}$ peak (Fig. 3e), three deconvoluted peaks are associated with Cu^0, Cu^{2+}, and Sat. Here, Cu^0 is from metallic Cu, while Cu^{2+} originates from the surface oxidized states or copper doping into the Co_xW_xC phases.[39,40] In comparison, the $R(Cu^0/Co^{2+})$ value of the

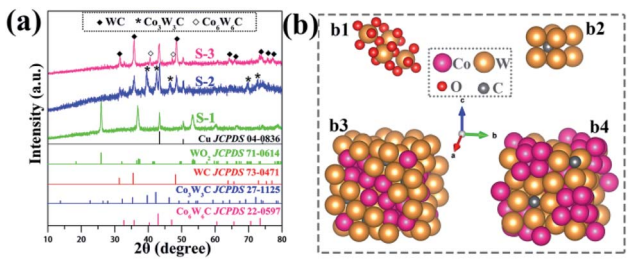

Fig. 2 (a) XRD patterns of the S-1, S-2, and S-3 samples; (b) the crystal structure: (b1) monoclinic WO_2, (b2) hexagonal WC, (b3) cubic Co_3W_3C, and (b4) cubic Co_6W_6C.

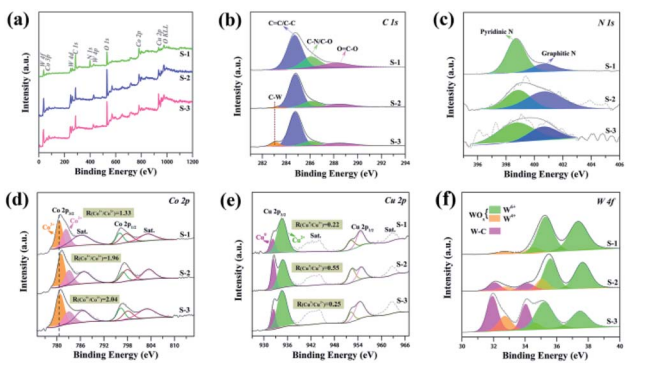

Fig. 3 X-ray photoelectron spectroscopy (XPS) of the S-1, S-2, and S-3 samples. (a) Survey spectra; high-resolution (HR)-XPS spectra of (b) C 1 s, (c) N 1 s, (d) Co 2p, (e) Cu 2p, (f) W 4f (*R* means the corresponding ratio).

S-2 sample reaches 0.55, which is 2.5 and 2.2 times as large as that of the S-1 and S-3 samples, respectively, proving that more low-valence-state Cu species are incorporated in the S-2 sample. The profile of W 4f in the S-1 sample can be fitted into four peaks involving the WO_x phases (W^{6+}: 37.4 and 35.3 eV; W^{4+}: 34.6 and 32.7 eV).[15] By contrast, a pair of additional peaks at around 34.1 and 32.0 eV can be observed in the W 4f profile of the S-2 and S-3 samples, which are in good agreement with the binding energy of W–C bonding.[17] Moreover, we also find that the relative content of high-valence-state W species (W^{6+}) decreases in the sequence S-1 (89%) < S-2 (67%) < S-3 (45%), which can convince us that abundant low-valence-state W species exist in the S-2 sample, thus providing more active sites for HER. According to the above-mentioned insights, we propose that the rational configuration of the Cu-Co-W system enables efficient electron transfer from Co to Cu and W; this results in a higher Co valence and lower Cu and W valence and is further conducive to the water splitting processes.[17,20,22,38]

In order to monitor the morphology and microstructure evolution of the samples prepared under different conditions, scanning electron microscopy (SEM) images and transmission electron microscopy (TEM) images were obtained. As shown in Fig. S3b (ESI†), such a relatively low reaction temperature of 700 °C is capable of making original small $CuWO_4$ nanoparticles agglomerate into irregular bulky particles of various sizes (S-4 sample). Correspondingly, the S-5 sample (Fig. S6, ESI†) exhibits a well-reserved polyhedral structure similar to that of ZIF-67. Plenty of confined metallic Co nanoparticles evenly distribute over the carbon polyhedron frame, indicating the superior confinement effect of the carbon polyhedron to prevent grains from growing infinitely. From the SEM images of the S-1, S-2, and S-3 samples (Fig. S7, ESI†), it is found that the initial core–shell polyhedral structure is gradually destroyed along with the increase in the reaction temperature. However, hardly any agglomerated particles with sizes in the micrometer scale are observed even though the sample is fabricated at a relatively high reaction temperature of 800 °C. This is definitely eligible to make the desirable confinement effect of the carbon polyhedron much more convincing.

The detailed structural evolution processes are further characterized by TEM. The S-1 sample, as shown in Fig. S8 (ESI†), exhibits an unbroken core–shell structure made up of interior WO_2 nanoparticles and exterior amorphous carbon shells with an average thickness of about 10.5 nm. With the enhancement in the reaction temperature, the external carbon layers become thinner and thinner, and their graphitization degree tends to increase as well. Until the reaction temperature reaches 800 °C, the as-fabricated S-3 sample possesses more distinct graphitic carbon fringes and massive congregated blocks inter-linked with numerous particles (Fig. S9, ESI†). For the S-2 sample, phase transformations from monoclinic WO_2 to hexagonal WC and subsequently to cubic Co_3W_3C with Cu doping can be achieved. Compared to the S-4 sample, the tendency to congregate into larger particles for WC and Cu-doped Co_3W_3C can be effectively restricted by carbon-supporting matrices, but both of them still show slightly greater grains relative to the WO_2 particles. In Fig. 4a, we can

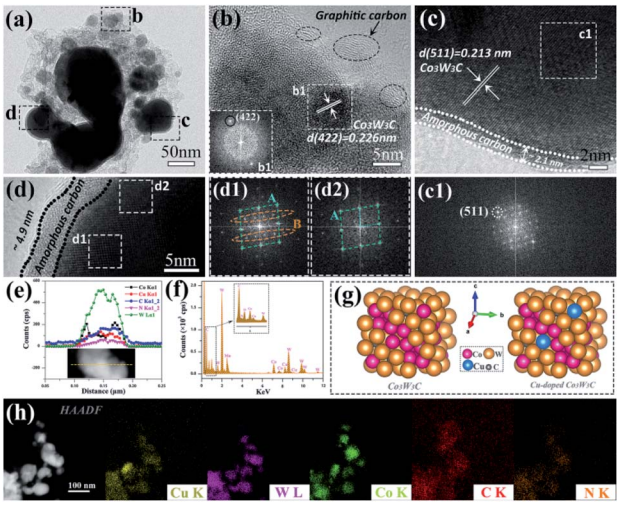

Fig. 4 (a) TEM image; (b–d) HRTEM images; (b1) (c1) (d1) and (d2) the corresponding FFT patterns; (e) EDS line-scan spectra along the dashed line on one particle; (f) EDS spectrum of the S-2 sample; (g) the crystal structure illustrations of Co_3W_3C and Cu-doped Co_3W_3C; (h) HAADF image and corresponding elemental mapping of the S-2 sample.

observe numerous dispersed nanoparticles among the whole carbon matrices. These particles can be basically divided into two parts: relatively small particles embedded into the supporting carbon skeleton and bulky grains coated with amorphous carbon layers. The specific structures around the particles are further examined by three selected amplificatory images (area b, c, and d). As viewed in Fig. 4b, the small particles having an inter-planar spacing of 0.226 nm, consistent with the (422) plane of cubic Co_3W_3C, are planted in the amorphous carbon matrices, meanwhile interconnecting with the outer graphitic carbon layer and collectively making up a conductive network. Similarly, the fast Fourier transform (FFT) algorithm pattern (b1) in Fig. 4b implies the existence of amorphous carbon and Co_3W_3C. On the other hand, one big particle with a coated carbon layer (thickness about 2.1 nm, Fig. 4c) presents the lattice spacing of 0.231 nm, which is indexed to the (511) plane of Co_3W_3C. This is in line with the results of the corresponding FFT pattern (Fig. 4c1). Another large particle displays the thickness of the capped carbon layer to be about 4.9 nm (Fig. 4d). Nevertheless, the FFT patterns originating from different parts of the particle have an obvious difference. In comparison to the FFT pattern of area d2, an additional set of diffraction spots are apparent in area d1, which means that this particle is composed of two phases. We think that this is caused by the interposition of Cu and Co atoms into the WC crystal, coinciding with the XPS results. Superficial component and elemental distribution are investigated by energy spectrum analysis. The energy-dispersive line-scan spectrum (Fig. 4e) and energy-dispersive spectra (EDS, Fig. 4f) both reveal the signals of the C, N, Cu, Co, and W elements. In particular, the most intensive signal of the as-collected elements is that of the W element, indicating that the elementary phases of S-2 contain ample W species. We notice that the relative concentration of

Co is distinctly improved at both ends of the particles, manifesting that more cubic Co_3W_3C species reside at the peripheral regions. This is attributed to a gradual infiltration process of the Co atoms into the lattice of WC to form Co_3W_3C interstitial compounds. Moreover, the Cu element is distributed uniformly throughout the scanning line, giving a reliable confirmation of the successful doping of Cu atoms into cubic Co_3W_3C. In consideration of the extremely similar atomic radii of Cu and Co, the Co sites in the Co_3W_3C phase can be easily replaced by Cu atoms, consequently forming the Cu-doped Co_3W_3C phase (the details of the crystal structures of Co_3W_3C and Cu-doped Co_3W_3C are given in Fig. 4g). Essentially, Cu-doped Co_3W_3C is a kind of compound in which metallic Cu and Co atoms are inserted into the interstitial voids of WC. As visual evidence, EDS elemental mapping enables us to identify the spatial distribution states of various elements. It can be known from Fig. 4h that the C, N, Cu, Co, and W elements are spread over the whole region of S-2. Based on these facts, we therefore propose that cubic metallic Cu not only merely maintains external contact with hexagonal WC and cubic Co_3W_3C, but also gets into the lattice spacing of Co_3W_3C by replacing the Co sites, which agrees well with the above-stated XRD analysis.

As is generally recognized, the specific surface area of catalysts is intimately associated with the amount of exposed active sites and mass transfer capability, which influence their catalytic performances. According to our previous reports, the carbon polyhedron would have a decreased specific surface area in contrast to its precursor MOFs.[41,42] Compared to S-3, the S-2 sample (Fig. S10, ESI†) has a higher specific surface area of 12.911 $m^2\ g^{-1}$ and pore volume of 0.024 $cm^3\ g^{-1}$. This will definitely be beneficial to expose more active centers and provide favorable charge transfer and gas transportation channels, finally contributing to higher electrocatalytic activities.[39,43]

3.2. OER and HER catalytic performances

The electrocatalytic activity of the as-synthesized nanohybrids was preliminarily evaluated by the oxygen evolution reaction (OER) under an O_2-saturated alkaline electrolyte (1 M KOH solution) with a standard three-electrode system. Fig. 5a shows the linear sweep voltammetry (LSV) curves of the as-developed samples and the commercial RuO_2 catalyst, in which the scan rate is 5 mV s^{-1} with 95% IR-compensation. As can be seen, the S-2 sample is the most active towards OER, just requiring the over-potentials (η) of 238 and 307 mV to achieve the current densities (j) of 10 and 100 mA cm^{-2}, respectively, which are much lower than those of the other counterparts: S-1 ($\eta_{j=10}$ = 256 mV and $\eta_{j=100}$ = 314 mV), S-3 ($\eta_{j=10}$ = 269 mV and $\eta_{j=100}$ = 367 mV), S-4 ($\eta_{j=10}$ = 444 mV and $\eta_{j=100}$ = 617 mV), S-5 ($\eta_{j=10}$ = 311 mV and $\eta_{j=100}$ = 403 mV), and commercial RuO_2 ($\eta_{j=10}$ = 278 mV and $\eta_{j=100}$ = 387 mV); these even surpass those of most reported relevant carbide catalysts (Table S4, ESI†). Involving multi-electron transfer steps and a series of oxygen-containing group conversions, OER is generally regarded as a key barrier limiting electrocatalytic water splitting due to its lack of favorable reaction kinetics.[44] The electrocatalytic kinetics of the as-developed catalysts was evaluated by Tafel plots, as shown in

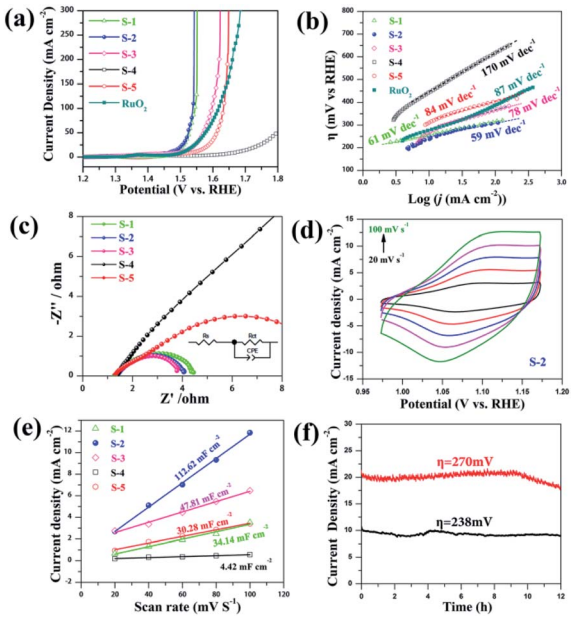

Fig. 5 Oxygen evolution reaction (OER) performances in 1 M KOH electrolyte. (a) LSV polarization curves; (b) the corresponding Tafel plots; (c) Nyquist plots, where the inset reveals the equivalent circuit diagram; (d) CV curves of the S-2 sample at different scanning rates; (e) the double-layer capacitance (C_{dl}); (f) current density–time (j–t) curves at η = 238 mV and 270 mV for 12 h.

Fig. 5b. The Tafel slope of 59 mV dec^{-1} for the S-2 sample is much smaller than those of S-1 (61 mV dec^{-1}), S-3 (78 mV dec^{-1}), S-4 (170 mV dec^{-1}), S-5 (84 mV dec^{-1}), and RuO_2 catalyst (87 mV dec^{-1}), demonstrating the most beneficial OER kinetics of the S-2 sample in a 1 M KOH solution.

Electrochemical impedance spectroscopy (EIS) (Fig. 5c) acts as a tool to figure out the interfacial charge transfer ability between catalysts and electrolytes, thus further investigating the OER kinetics. The data were obtained at an overpotential of 340 mV with an AC amplitude of 5 mV. After fitting with the inserted model, the charge transfer resistance (R_{ct}) of the S-2 electrode (Table S5, ESI†) was 2.74 Ω, which was similar to that of the S-3 sample (2.72 Ω) but quite lower than the R_{ct} values of S-1 (3.32 Ω), S-4 (60.31 Ω), and S-5 (11.16 Ω), indicating that the S-2 sample has superior charge transfer ability.[2,45] Note that the R_{ct} values of the S-2 and S-3 samples are very close to each other but both are much smaller than that of the S-1 sample as we are aware that the main phase differences among the S-1, S-2, and S-3 samples are W-based compounds, namely, tungsten in S-2 and S-3 exists in the form of hexagonal WC and Cu-doped Co_xW_xC, and S-1 consists of semiconductor WO_2 instead. Therefore, better electro-conductibility could be achieved in the S-2 and S-3 samples. As we know, the electrochemical active surface area (ECSA) of catalysts has obviously positive correlation with the double-layer capacitance (C_{dl}).[46] Herein, the C_{dl} values are obtained by the CV method (Fig. 5d and S11†). As shown in Fig. 5e, the C_{dl} value of the S-2 sample is as high as 112.62 mF cm^{-2}, which is about 4 and 3 times as large as that of the S-1 (34.14 mF cm^{-2}) and S-3 samples (47.81

mF cm^{-2}). Benefitting from the relatively high surface area and larger C_{dl} value of the S-2 sample, more exposed surface active sites and accelerated charge transfer as well as gas transportation ability can be realized, which are subsequently responsible for its best OER activity.[47] Apart from high activity, the desirable stability of the S-2 sample towards OER is also confirmed by the long-term current density–time (j–t) curves at different applied potentials (Fig. 5f). The current density losses at $\eta_{j=10}$ = 238 mV and $\eta_{j=20}$ = 270 mV are only 9% and 11%, respectively, indicating the acceptable electrochemical stability of the S-2 sample in alkaline media, which comes from the effective protective effect of the coated carbon layer and supporting carbon matrices as well as the good electrochemical stability of Cu-doped Co_3W_3C.[17,48]

Likewise, experiments to assess the electrochemically catalyzed HER performances of all the prepared samples were carried out in 1 M N_2-saturated KOH electrolytes at room temperature. Just as expected, commercial 20 wt% Pt/C exhibited the best behavior for HER with an overpotential of just 73 mV to afford a current density of 10 mA cm^{-2}. It is evident from Fig. 6a and c that the S-2 sample exhibits excellent catalytic activity with an overpotential of 98 mV at a current density of 10 mA cm^{-2}; this is slightly inferior to that of the commercial 20 wt% Pt/C catalyst but quite superior to that of the S-1 (137 mV), S-3 (125 mV), S-4 (181 mV), and S-5 (141 mV) samples and most of the reported metal carbide catalysts (Table S6, ESI†). Even at larger current density, the S-2 sample showed the best performance among the other reference samples, indicating its more favorable mass transfer and reaction kinetics. For HER, the underlying catalytic kinetics and reaction pathways of the catalysts could be disclosed by their corresponding Tafel slopes. The Tafel slope (Fig. 6b) of S-2 is 50 mV dec^{-1}, which is comparable to that of commercial 20 wt% Pt/C catalyst (49 mV dec^{-1}) and exceeds that of the other as-obtained samples. This fact certifies the outstanding HER catalytic kinetics of nitrogen-doped carbon-supported polymetallic carbide hybrids (S-2 sample) in alkaline media.[33] The value of the Tafel slope for the S-2 sample ranges between 40 mV dec^{-1} and 120 mV dec^{-1}, suggesting that it is dominated by the Volmer–Heyrovsky mechanism,[18] where $H_2O + e^- \rightarrow H_{ads} + OH^-$ (Volmer) and $H_{ads} + H_2O + e^- \rightarrow H_2 + OH^-$ (Heyrovsky) are the rate-determining steps throughout the HER processes. Moreover, we measured the charge transfer resistance value (R_{ct}) of the as-fabricated catalysts in the HER process *via* EIS. The lowest R_{ct} value (5.38 Ω) of the S-2 catalyst, presented in Fig. 6d and Table S5 (ESI†), is associated with the most rapid charge transfer in the S-2/Ni foam electrode.[3] This tendency coincides with the data measured in the OER processes, and both of them result from the established benign charge transfer channels of the Cu-Co-W-C-N components.[48] Not only praiseworthy HER activity, but also the good sustainability of the S-2 catalyst is revealed by the chronoamperometry (j–t curve) measurements. As seen from Fig. 6e, the drop in the current density is about 10% after continuous operation for 12 h with an applied potential of 122 mV, which is likely attributed to the adsorption of hydrogen bubbles onto the electrode surface and loss of some catalysts by overflowing bubbles. Moreover, the potential gaps between $\eta^{OER}_{j=10}$ and $\eta^{HER}_{j=10}$ for the as-developed catalysts and the pair of commercial 20 wt% Pt/C and RuO_2 catalysts were calculated through two half-cell reactions of water splitting in 1 M KOH (Fig. 6f). The calculated gap value of the S-2 catalyst is 1.566 V (Table S8, ESI†), which is better than that of the pair of Pt/C and RuO_2 (1.581 V), thus further supporting its first-class electrocatalytic water splitting performance.[2]

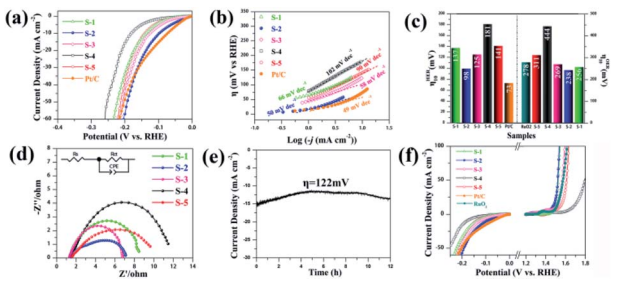

Fig. 6 Hydrogen evolution reaction (HER) tests in 1 M KOH. (a) LSV polarization curves; (b) the corresponding Tafel plots; (c) the histogram to describe $\eta_{j=10}$ values of all the samples for OER and HER; (d) Nyquist plots, where the inset represents the equivalent circuit diagram; (e) HER stability tests by long-term current density–time (j–t) curves; (f) LSV curves of all the samples for OER and HER.

3.3. Analysis of active components and catalytic mechanism

To better understand the water splitting activities of the nitrogen-doped carbon-hosted polymetallic carbide catalysts, in-depth analysis of the active components and catalytic mechanism in this system is made as given below. Several previous studies have confirmed the affirmative impact of constructing transition metal/carbide (Ni/Mo_xC,[20,22] Co/Mo_xC,[21] and Ni/WC[19]) interfaces on both the HER and OER performances. In particular, K. K. Nanda *et al.*[20] developed a kind of N-doped graphene/CNT-supported Ni/Mo_xC hybrid (Ni-Mo_xC/NC-100) by annealing nickel molybdate nanorods and melamine. They ascribed the high-performance electrocatalytic activity of Ni-Mo_xC/NC-100 to the electronic synergistic effect among self-included Mo_xC, metallic Ni, and N-doped graphene/CNT, especially highlighting that the beneficial alteration of hydrogen and water adsorption energy towards the Mo_xC phase arises from electron transfer from metallic Ni to Mo_xC. On the basis of these findings, a handful of studies alternatively aimed at the direct construction of M_xN_xC (M = Fe/Co/Ni, N = Mo/W, x = 3/6) for electrochemical water splitting,[23,26,27,34,37] adequately proving their authentic and effective catalytic activity and durability. In our catalyst systems, W in the S-1 sample exists in the form of WO_2. In contrast, it is transformed into tungsten carbide-based compounds for the S-2 and S-3 samples, which means that the chemical environment and electron density around the W sites are completely different.[19] As measured, the S-2 sample consists of metallic Cu, hexagonal WC, Cu-doped Co_3W_3C, and nitrogen-doped carbon. Herein, Cu-doped Co_3W_3C could be regarded as a phase that was generated by inserting Cu and Co atoms into the interstitial voids of WC.

Structural and compositional analyses confirm that both the Cu and Co atoms are closely linked with the tungsten carbide species. Hence, effective electronic interactions can be generated among different components and chemical structures. Specifically, the insights into the XPS spectra of Co 2p, Cu 2p, and W 4f demonstrate that abundant high-valence-state Co^{3+} and low-valence-state Cu and W species exist in the S-2 sample (Fig. 3), which is ascribed to the local electronic structure reconfiguration. In other words, the suitable distributions of Cu and Co onto the WC nanocrystals are able to trigger the beneficial electron transfer from Co to Cu and W, resulting in elemental valence state changes in Co, Cu, and W.[2,22,46] As an additional support, the electronegativity values of the Co, Cu, W, C, and N atoms are 1.88, 1.90, 2.36, 2.55, and 3.04, respectively, further endowing these achievements of electron transfer. More high-valence-state cobalt ions are generally responsible for better OER properties;[49] however, electron-rich and low-valence-state tungsten species are capable of yielding high-performance HER activity owing to their similar d-band electronic configuration to that of Pt.[50] As an experimental reflection, the S-2 catalyst electrode shows low interfacial charge resistance for both OER and HER. Good electrical conductivity, large surface area, and pore volume are other advantages of the S-2 catalyst. Herein, we highlight that Cu plays a significant role in material preparation and catalytic reactions. Unlike some other reports,[17,21] metallic phase Co is absent for the as-obtained S-1, S-2, and S-3 catalysts. The reason is that the presence of Cu with slightly higher electronegativity prevents the generation of metallic Co in synthetic procedures and facilitates the successful insertion of metallic Co into the lattice of WC, which is finally responsible for the production of Cu-doped Co_3W_3C. In a real catalytic operation, metallic Cu not only serves as a good conductor to endow decent electrical conductivity, but also restricts Co species from being reduced; it also acts as a bridge to achieve electron transfer to the W sites. Thus, the existence of Cu is crucial for good overall water splitting activities.

Mass activity and turnover frequency (TOF) values by supposing different metals (Co and W) as active sites for the OER and HER processes were calculated (Fig. 7), which are conducive for disclosing the catalytically active sites.[51] As shown in Fig. 7b, the S-2 catalyst exhibits the largest mass activity and TOF values at any identical overpotentials (η) by assuming total Co atoms as the catalytically active sites when used as OER catalysts. In detail, the S-2 catalyst could afford the mass activity and TOF values (Fig. 7c) of 13.93 A g^{-1} and 0.0176 s^{-1} at η = 280 mV, respectively, which were much higher than those of the S-1 catalyst (mass activity = 12.48 A g^{-1}; TOF_{Co}^{OER} = 0.0113 s^{-1}), S-3 catalyst (mass activity = 5.98 A g^{-1}; TOF_{Co}^{OER} = 0.0095 s^{-1}), and commercial RuO_2 catalyst (mass activity = 5.32 A g^{-1}; TOF_{Ru}^{OER} = 0.0011 s^{-1}, supposing Ru atoms as active sites). This adequately testifies that Co sites are the main catalytically active sites for OER. With regard to HER, the mass activity of the S-2 catalyst (Fig. 7d) was superior to that of any other as-synthesized catalyst and even exceeded that of the 20 wt% Pt/C catalyst at an overpotential of more than 169 mV. The TOF_W value of the S-2 catalyst (Fig. 7e) reaches 0.0091 s^{-1} at a low overpotential of 100 mV, which is better than that of the S-1 catalyst (TOF_W = 0.0085 s^{-1}) and S-3 catalyst (TOF_W = 0.0055 s^{-1}), suggesting that the W atoms are the active sites for HER. Combined with the above-stated structure and component analyses and TOF calculations, we believe that this benign dual transition metallic source modification of tungsten carbide nanocrystals by copper and cobalt to regulate the local electronic structure has the qualified ability to beneficially change the chemical environment around the W sites and Co sites in the as-developed nanohybrid system, making the catalyst conducive for creating abundant catalytically active sites for both OER and HER. In this case, the as-fabricated S-2 sample is highly expected to be a promising catalyst for electrochemical overall water splitting.

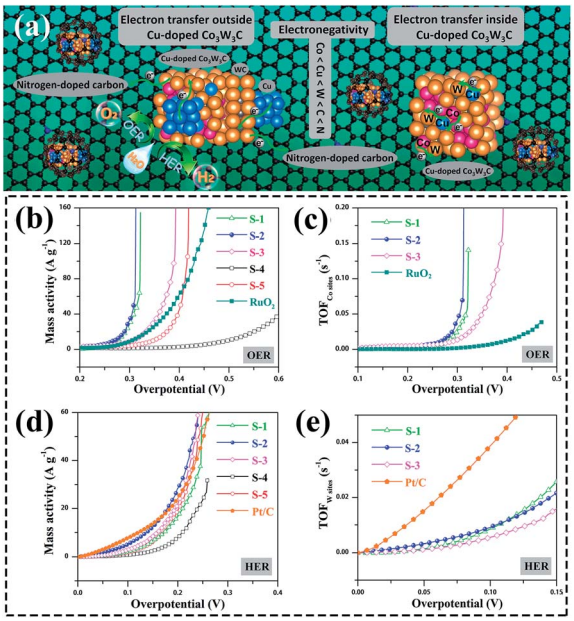

Fig. 7 (a) The illustration of proposed electron transfer mechanism of the S-2 catalyst; the calculated mass activity of the samples for OER (b) and HER (d); turnover frequency (TOF) values by assuming the whole surface Co atoms (c) and W atoms (e) as active sites for OER and HER, respectively.

3.4. Overall water splitting

Encouraged by the impressive HER and OER activities in alkaline media, a home-made electrochemical electrolyzer integrated with two S-2 catalyst electrodes (denoted as S-2//S-2) as the cathode and anode was assembled to assess the ability of overall water splitting,[52–54] in which the apparent hydrogen and oxygen bubbles could be observed on two separated S-2 electrodes, as shown in a digital photograph (Fig. 8a). The as-made S-2//S-2 electrolyzer (Fig. 8b) can achieve a current density of 10 mA cm^{-2} at an applied voltage of merely 1.64 V for overall water splitting, which is comparable to and even higher than those of many reported carbide electrocatalysts (inset of Fig. 8b). In addition, the S-2//S-2 couple electrodes are capable of maintaining satisfactory stability under diverse current densities (~10 and 18 mA cm^{-2} correspond to the potentials of 1.64 V and

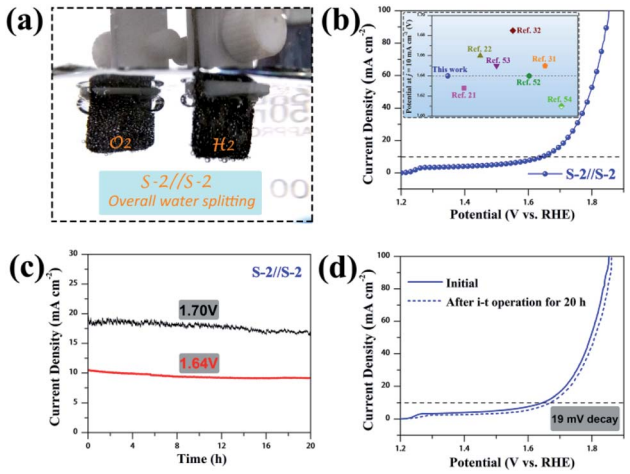

Fig. 8 Overall water splitting tests for the S-2 sample in 1 M KOH: (a) digital photograph of the home-made water splitting device, (b) LSV curve, (c) current density–time (j–t) stability tests at different applied potentials (AP), (d) LSV curves before and after stability tests at an AP of 1.64 V.

1.70 V), showing the current density retention rates of 91.4% and 88.7% (Fig. 8c), respectively. The good stability of the S-2 catalyst electrodes could be further demonstrated by the LSV curves (Fig. 8d) before and after long-term stability tests at 1.64 V for 20 h, exhibiting a potential decay of only 19 mV at the current density of 10 mA cm^{-2}, which convincingly illustrated its high electrochemical stability.[55] This means that nitrogen-doped carbon-supported Cu-doped Co_3W_3C has an extremely promising future to be the practical and economical overall water splitting catalyst for long-term industrial operation.

4 Conclusions

In summary, we developed nitrogen-doped carbon-hosted metallic carbide as a high-efficiency and durable alkaline water splitting catalyst by annealing the core–shell $CuWO_4$@-ZIF-67 structure under an argon atmosphere. The as-synthesized S-2 catalyst essentially comprised nitrogen-doped carbon matrix-hosted metallic Cu, hexagonal WC, and Cu-doped Co_3W_3C. Herein, the introduction of Cu could prevent the formation of metallic phase Co in the synthesis process. On the other hand, tungsten carbide nanocrystals dual-modified with the transition metals copper and cobalt could drive electron transfer in the order Co → Cu → W for the as-fabricated sophisticated NC@Cu-Co-W-C system, leading to abundant high-valence-state Co^{3+} and low-valence-state Cu and W species in the S-2 catalyst. With these plentiful catalytically active sites, it only requires the η values of 238 mV and 98 mV to achieve j_{10} for OER and HER, respectively, outperforming most state-of-the-art metal carbide catalysts. The home-made S-2//S-2 electrolyzer just needed a cell potential of 1.64 V to launch j_{10}. The satisfactory stability for various catalytic measurements was also demonstrated by the long-term j–t operations. Last but not the least, the mass activity and TOF calculations revealed that the Co and W species served as active sites for OER and HER, respectively. This work highlights the positive influence of the local electronic structure reconfiguration on enhanced electrochemical water splitting performances and sheds new light on the rational design and synthesis of active and durable molybdenum/tungsten carbide electrocatalysts by introducing appropriate transition metals.

Conflicts of interest

There are no conflicts to declare.

Acknowledgements

This work is financially supported by the National Natural Science Foundation of China (Grant No. 11674398). The authors thank the Electron Microscopy Laboratory in Peking University for the use of FEI Tecnai G2 F20.

Notes and references

1 Z.-H. Xue, H. Su, Q.-Y. Yu, B. Zhang, H.-H. Wang, X.-H. Li and J.-S. Chen, *Adv. Energy Mater.*, 2017, **7**, 1602355.
2 G.-F. Chen, T. Y. Ma, Z.-Q. Liu, N. Li, Y.-Z. Su, K. Davey and S.-Z. Qiao, *Adv. Funct. Mater.*, 2016, **26**, 3314–3323.
3 C. Wu, D. Liu, H. Li and J. Li, *Small*, 2018, **14**, 1704227.
4 Q. Qin, J. Hao and W. Zheng, *ACS Appl. Mater. Interfaces*, 2018, **10**, 17827–17834.
5 B. Ren, D. Li, Q. Jin, H. Cui and C. Wang, *J. Mater. Chem. A*, 2017, **5**, 13196–13203.
6 D. Zhou, Z. Cai, X. Lei, W. Tian, Y. Bi, Y. Jia, N. Han, T. Gao, Q. Zhang, Y. Kuang, J. Pan, X. Sun and X. Duan, *Adv. Energy Mater.*, 2018, **8**, 1701905.
7 Q. Qin, H. Jang, L. Chen, G. Nam, X. Liu and J. Cho, *Adv. Energy Mater.*, 2018, **8**, 1801478.
8 L. C. Seitz, C. F. Dickens, K. Nishio, Y. Hikita, J. Montoya, A. Doyle, C. Kirk, A. Vojvodic, H. Y. Hwang, J. K. Norskov and T. F. Jaramillo, *Science*, 2016, **353**, 1011–1014.
9 Z. Kou, L. Zhang, Y. Ma, X. Liu, W. Zang, J. Zhang, S. Huang, Y. Du, A. K. Cheetham and J. Wang, *Appl. Catal., B*, 2019, **243**, 678–685.
10 Y. Hu, B. Yu, W. Li, M. Ramadoss and Y. Chen, *Nanoscale*, 2019, **11**, 4876–4884.
11 X. Xu, F. Nosheen and X. Wang, *Chem. Mater.*, 2016, **28**, 6313–6320.
12 W. Cui, N. Cheng, Q. Liu, C. Ge, A. M. Asiri and X. Sun, *ACS Catal.*, 2014, **4**, 2658–2661.
13 S. Wang, J. Wang, M. Zhu, X. Bao, B. Xiao, D. Su, H. Li and Y. Wang, *J. Am. Chem. Soc.*, 2015, **137**, 15753–15759.
14 X. J. Fan, H. Q. Zhou and X. Guo, *ACS Nano*, 2015, **9**, 5125–5134.
15 Z. Y. Chen, L. F. Duan, T. Sheng, X. Lin, Y. F. Chen, Y. Q. Chu, S. G. Sun and W. F. Lin, *ACS Appl. Mater. Interfaces*, 2017, **9**, 20594–20602.
16 Q. Gao, W. Zhang, Z. Shi, L. Yang and Y. Tang, *Adv. Mater.*, 2019, **31**, 1802880.
17 H. Jin, J. Chen, S. Mao and Y. Wang, *ACS Appl. Mater. Interfaces*, 2018, **10**, 22094–22101.

18 L.-N. Zhang, Y.-Y. Ma, Z.-L. Lang, Y.-H. Wang, S. U. Khan, G. Yan, H.-Q. Tan, H.-Y. Zang and Y.-g. Li, *J. Mater. Chem. A*, 2018, **6**, 15395–15403.
19 Y.-Y. Ma, Z.-L. Lang, L.-K. Yan, Y.-H. Wang, H.-Q. Tan, K. Feng, Y.-J. Xia, J. Zhong, Y. Liu, Z.-H. Kang and Y.-G. Li, *Energy Environ. Sci.*, 2018, **11**, 2114–2123.
20 D. Das, S. Santra and K. K. Nanda, *ACS Appl. Mater. Interfaces*, 2018, **10**, 35025–35038.
21 L. Ai, J. Su, M. Wang and J. Jiang, *ACS Sustainable Chem. Eng.*, 2018, **6**, 9912–9920.
22 Z. Y. Yu, Y. Duan, M. R. Gao, C. C. Lang, Y. R. Zheng and S. H. Yu, *Chem. Sci.*, 2017, **8**, 968–973.
23 C. Y. He and J. Z. Tao, *Adv. Sustainable Syst.*, 2018, **2**, 1700136.
24 C. Chen, A. Wu, H. Yan, Y. Xiao, C. Tian and H. Fu, *Chem. Sci.*, 2018, **9**, 4746–4755.
25 M. Y. Zu, P. F. Liu, C. Wang, Y. Wang, L. R. Zheng, B. Zhang, H. Zhao and H. G. Yang, *ACS Energy Lett.*, 2017, **3**, 78–84.
26 C. He and J. Tao, *J. Catal.*, 2017, **347**, 63–71.
27 Z. Cui, Y. Li, G. Fu, X. Li and J. B. Goodenough, *Adv. Mater.*, 2017, **29**, 1702385.
28 M. Zeng, Y. Chen, J. Li, H. Xue, R. G. Mendes, J. Liu, T. Zhang, M. H. Rümmeli and L. Fu, *Nano Energy*, 2017, **33**, 356–362.
29 G. Yan, C. Wu, H. Tan, X. Feng, L. Yan, H. Zang and Y. Li, *J. Mater. Chem. A*, 2017, **5**, 765–772.
30 Y. T. Xu, X. Xiao, Z. M. Ye, S. Zhao, R. Shen, C. T. He, J. P. Zhang, Y. Li and X. M. Chen, *J. Am. Chem. Soc.*, 2017, **139**, 5285–5288.
31 Z. Yu, Y. Bai, S. Zhang, Y. Liu, N. Zhang, G. Wang, J. Wei, Q. Wu and K. Sun, *ACS Appl. Mater. Interfaces*, 2018, **10**, 6245–6252.
32 Q. Liang, H. Jin, Z. Wang, Y. Xiong, S. Yuan, X. Zeng, D. He and S. Mu, *Nano Energy*, 2019, **57**, 746–752.
33 S. Li, C. Cheng, A. Sagaltchik, P. Pachfule, C. Zhao and A. Thomas, *Adv. Funct. Mater.*, 2019, **29**, 1807419.
34 Y. Liu, G. D. Li, L. Yuan, L. Ge, H. Ding, D. Wang and X. Zou, *Nanoscale*, 2015, **7**, 3130–3136.
35 R. Dang, X. Jia, X. Liu, H. Ma, H. Gao and G. Wang, *Nano Energy*, 2017, **33**, 427–435.
36 I. Jeong, J. Lee, K. L. Vincent Joseph, H. I. Lee, J. K. Kim, S. Yoon and J. Lee, *Nano Energy*, 2014, **9**, 392–400.
37 C. He and J. Tao, *Mater. Today Energy*, 2018, **8**, 65–72.
38 C. Wan and B. M. Leonard, *Chem. Mater.*, 2015, **27**, 4281–4288.
39 J. Zheng, X. Chen, X. Zhong, S. Li, T. Liu, G. Zhuang, X. Li, S. Deng, D. Mei and J.-G. Wang, *Adv. Funct. Mater.*, 2017, **27**, 1704169.
40 M. Kuang, Q. Wang, P. Han and G. Zheng, *Adv. Energy Mater.*, 2017, **7**, 1700193.
41 L. Qiao, A. Zhu, H. Yang, W. Zeng, R. Dong, P. Tan, D. Zhong, Q. Ma and J. Pan, *Inorg. Chem. Front.*, 2018, **5**, 2276–2283.
42 L. Qiao, A. Zhu, Y. Liu, Y. Bian, R. Dong, D. Zhong, H. Wu and J. Pan, *J. Mater. Sci.*, 2018, **10**, 7755–7766.
43 Z. Cheng, Q. Fu, Q. Han, Y. Xiao, Y. Liang, Y. Zhao and L. Qu, *Adv. Funct. Mater.*, 2018, **28**, 1705967.
44 H. N. Nong, T. Reier, H.-S. Oh, M. Gliech, P. Paciok, T. H. T. Vu, D. Teschner, M. Heggen, V. Petkov, R. Schlögl, T. Jones and P. Strasser, *Nat. Catal.*, 2018, **1**, 841–851.
45 X. Zhang, H. Xu, X. Li, Y. Li, T. Yang and Y. Liang, *ACS Catal.*, 2015, **6**, 580–588.
46 H. Lin, N. Liu, Z. Shi, Y. Guo, Y. Tang and Q. Gao, *Adv. Funct. Mater.*, 2016, **26**, 5590–5598.
47 Y. Zhou, R. Ma, P. Li, Y. Chen, Q. Liu, G. Cao and J. Wang, *J. Mater. Chem. A*, 2016, **4**, 8204–8210.
48 J. Su, G. Xia, R. Li, Y. Yang, J. Chen, R. Shi, P. Jiang and Q. Chen, *J. Mater. Chem. A*, 2016, **4**, 9204–9212.
49 B. Zhang, X. Zheng, O. Voznyy, R. Comin, M. Bajdich, M. García-Melchor, L. Han, J. Xu, M. Liu, L. Zheng, F. Pelayo García de Arquer, C. Thang Dinh, F. Fan, M. Yuan, E. Yassitepe, N. Chen, T. Regier, P. Liu, Y. Li, P. De Luna, A. Janmohamed, H. L. Xin, H. Yang, A. Vojvodic and E. H. Sargent, *Science*, 2016, **352**, 333–337.
50 Y. Shen, L. Li, J. Xi and X. Qiu, *J. Mater. Chem. A*, 2016, **4**, 5817–5822.
51 M. Gao, W. Sheng, Z. Zhuang, Q. Fang, S. Gu, J. Jiang and Y. Yan, *J. Am. Chem. Soc.*, 2014, **136**, 7077–7084.
52 S. Dutta, A. Indra, H. Han and T. Song, *ChemSusChem*, 2018, **11**, 3956–3964.
53 J. Xing, Y. Li, S. Guo, T. Jin, H. Li, Y. Wang and L. Jiao, *Electrochim. Acta*, 2019, **298**, 305–312.
54 X. Luo, Q. Zhou, S. Du, J. Li, J. Zhong, X. Deng and Y. Liu, *ACS Appl. Mater. Interfaces*, 2018, **10**, 22291–22302.
55 H. Zhang, Q. Pan, Z. Sun and C. Cheng, *Nanoscale*, 2019, **11**, 11505–11512.

